

# Cu<sub>2</sub>O–Cu@Titanium Surface with Synergistic Performance for Nitrate-to-Ammonia Electrochemical Reduction

Marcelo Eduardo Chavez, Martí Biset-Peiró, Sebastián Murcia-López,\* and Joan Ramon Morante

Cite This: *ACS Sustainable Chem. Eng.* 2023, 11, 3633–3643

Read Online

ACCESS |



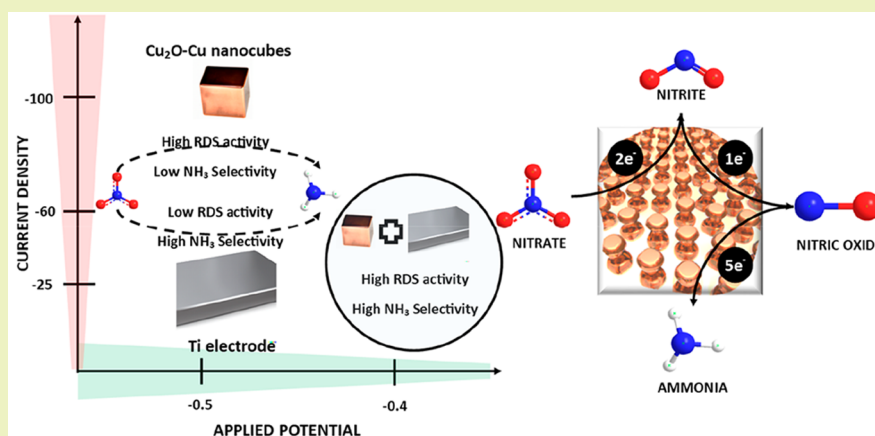
Metrics &amp; More



Article Recommendations



Supporting Information



**ABSTRACT:** Transition metals, such as titanium (Ti) and copper (Cu) along with their respective metal oxides (TiO<sub>2</sub>, Cu<sub>2</sub>O, and CuO), have been widely studied as electrocatalysts for nitrate electrochemical reduction with important outcomes in the fields of denitrification and ammonia generation. Based on this, this work conducted an evaluation of a composite electrode that integrates materials with different intrinsic activities (i.e., Cu and Cu<sub>2</sub>O for higher activity for nitrate conversion; Ti for higher faradaic efficiency to ammonia) looking for potential synergistic effects in the direction of ammonia generation. The specific performance of single-metal and composite electrodes has shown a strong dependence on pH and nitrate concentration conditions. Faradaic efficiency to ammonia of 92% and productivities of 0.28 mmol<sub>NH<sub>3</sub></sub>·cm<sup>-2</sup>·h<sup>-1</sup> at 0.5 V vs reversible hydrogen electrode (RHE) values are achieved, demonstrating the implicit potential of this approach in comparison to direct N<sub>2</sub>RR with values in the order of μmol<sub>NH<sub>3</sub></sub>·h<sup>-1</sup>·cm<sup>-2</sup>. Finally, the electrochemical rate constants (*k*) for Ti, Cu, and Cu<sub>2</sub>O-Cu/Ti disk electrodes were determined by the Koutecky–Levich analysis with a rotating disk electrode (RDE) in 3.02 × 10<sup>-6</sup>, 3.88 × 10<sup>-4</sup>, and 4.77 × 10<sup>-4</sup> cm·s<sup>-1</sup> demonstrating an apparent synergistic effect for selective NiRR to ammonia with a Cu<sub>2</sub>O-Cu/Ti electrode.

**KEYWORDS:** Nitrate electroreduction, Ammonia, Copper, Copper oxide, Titanium, Electrochemical rate constant

## INTRODUCTION

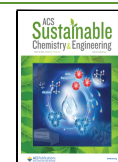
The energy transition and a hydrogen-based economy depend on the availability of energy in forms that allow long-term storage and transport from remote areas with an abundance of renewable energy (RE) sources, and liquefied forms are the preferred option.<sup>1</sup> Ammonia (NH<sub>3</sub>) is one of the more versatile commodities in the chemical industry, serving as a building block for the manufacture of many products, including fertilizers, plastics, explosives, textiles, and other chemicals.<sup>2</sup> Nonetheless, in addition to these applications in industry, NH<sub>3</sub> can play a relevant role as an energy vector due to several characteristics such as (i) being highly energy-dense;<sup>3</sup> (ii) being well-suited for large-scale energy transport applications;<sup>4</sup> (iii) being a zero-carbon hydrogen carrier;<sup>5</sup> (iv) being suitable for direct use as a zero-emission fuel for power applications in

fuel cells or a variety of engines.<sup>6</sup> Unfortunately, NH<sub>3</sub> actual production is based on the high energy-intensive Haber-Bosch process, combining nitrogen from the air and hydrogen from fossil fuels at high pressures and temperatures. This leads, therefore, to the emission of huge amounts of greenhouse gases (approximately 2.4 tons of carbon dioxide released into the atmosphere per ton of produced NH<sub>3</sub>) and as well a high energy consumption (approximately 2% of the total worldwide

**Received:** September 30, 2022

**Revised:** January 26, 2023

**Published:** February 22, 2023



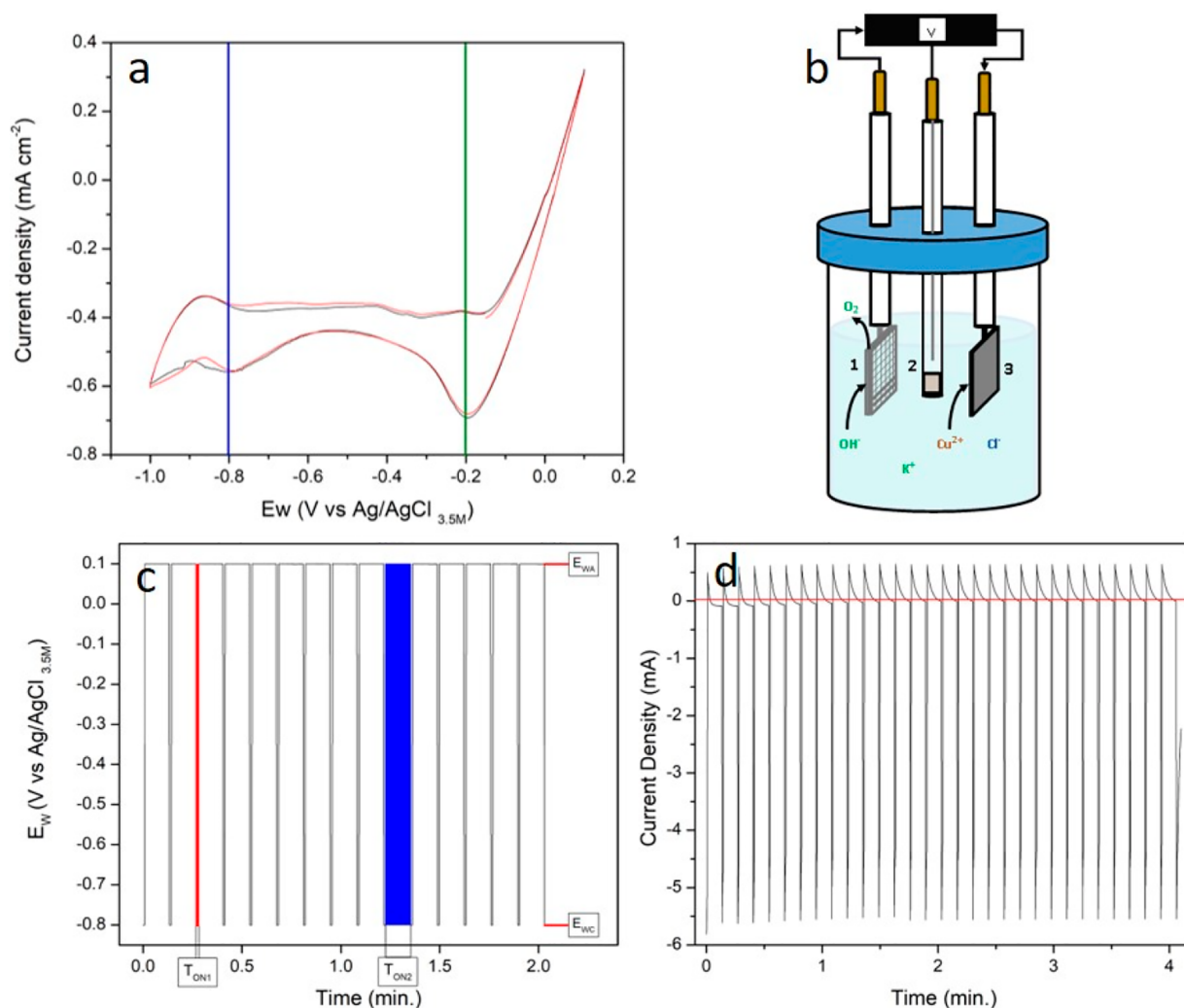


**Figure 1.** a) Cyclic Voltammetry 5 mM  $\text{CuCl}_2$  + 5 mM KCl electrolyte, pH 5.5–6; b) undivided three-electrode cell (1) platinum counter electrode, (2) Ag/AgCl 3.5 M KCl reference electrode, and (3) working electrode (Ti or Graphite foil); c) pulsed conditions ( $E_W$  and pulse time), and d) Chronoamperometry during PED.

energy consumption).<sup>7</sup> Nevertheless, the current demand for this chemical makes abandoning the Haber-Bosch process unlikely in the short term. In the lead of reducing the impact of  $\text{NH}_3$  production, a great interest has been triggered in some alternative routes including plasma catalysis and electrocatalysis.<sup>8,9</sup> Direct electrosynthesis of  $\text{NH}_3$  from  $\text{N}_2$  ( $\text{N}_2\text{RR}$ ),  $\text{H}_2\text{O}$ , and RE has the potential to simplify the entire process, to be easily implemented in isolated and remote areas. However, the initial  $\text{N}_2$  adsorption and first electron transfer steps have intrinsic high-energy barriers, which might favor competing HER and impact the final  $\text{NH}_3$  productivity (on the order of  $\mu\text{g}_{\text{NH}_3} \cdot \text{h}^{-1} \cdot \text{cm}^{-2}$ ).<sup>10,11</sup> As an alternative, nitrogen-oxyanions such as nitrates ( $\text{NO}_3^-$ ), mostly present as dissolved anions in polluted water from industrial sources, domestic sewage, sodium nitrate ore, and nitrification of bacteria,<sup>12,13</sup> constitute a promising nitrogen source to synthesize  $\text{NH}_3$  via the electrochemical route (NiRR). This route has the potential to achieve higher productivity values, as mass transfer limitations and inherent stability of molecular  $\text{N}_2$  are avoided, while at the same time constituting an environmental remediation strategy. The NiRR has been studied using several noble metals such as silver, gold, palladium, and ruthenium.<sup>14,15</sup>

However, the prohibitive costs of these materials make them less competitive for applications further than fundamental studies at the laboratory scale.<sup>16</sup> Other pure and combined transition metals have been also studied, among which copper (Cu) and iron (Fe) at different oxidation states<sup>17–20</sup> stand out as highly active materials for nitrate electroreduction by modification of shape, crystallographic orientation, and oxidation state, being either used as a single catalyst or in composite electrodes. Fu et al. have synthesized Cu nanosheets to maximize the efficiency of NiRR toward  $\text{NH}_3$ , reaching a faradaic efficiency to ammonia ( $\text{FE}_{\text{NH}_3}$ ) of 99.7% and studied the effects of changing catalyst shape in  $\text{FE}_{\text{NH}_3}$ .<sup>21</sup> Oxidized forms of Cu have demonstrated to enhance activity for NiRR. Fu et al. have studied how the interface  $\text{Cu}_2\text{O}-\text{Cu}$  alleviates the adsorption energy of  $\text{NO}_2^-$  and improves its diffusion.<sup>22</sup> Chen et al. have incorporated Cu nanoparticles onto an organic semiconductor busting the NiRR toward the  $\text{NH}_3$  reaction by regulating the proton/electrons flow to Cu centers.<sup>23</sup> Shih et al. have reported the effects on selectivity toward different nitrogen-based products of crystalline morphology of Cu nanoparticles on composite electrodes.<sup>24</sup> In fact, Cu selectivity is not limited to ammonia

generation. Several studies have been carried out with Cu-based materials, demonstrating its potential for water denitrification ( $\text{NO}_3^-$  to  $\text{N}_2$ ) and achieving  $\text{N}_2$  selectivity values close to 100%,<sup>25–27</sup> due its high ability of promoting the rate determinant step (RDS) of the overall NiRR. This intrinsic property of Cu made it an excellent primary catalyst if it is combined with other materials that can conduct NiRR toward ammonia generation after surpassing the RDS.

Ti-based electrodes have also recently attracted the attention of researchers due their high efficiency and stability under extreme electrochemical conditions. McEnaney et al. have reached a 90%  $\text{FE}_{\text{NH}_3}$  and 80% of selectivity ( $\text{SE}_{\text{NH}_3}$ ) with a pure Ti electrode applying electrolyte engineering.<sup>28</sup> Meanwhile, oxidized forms of Ti have also shown catalytic properties. Jia et al. boosted the selectivity toward  $\text{NH}_3$  by using  $\text{TiO}_2$  nanotubes with rich oxygen vacancies.<sup>29</sup> Consequently, the high selectivity of Ti electrodes for NiRR toward  $\text{NH}_3$  makes them suitable active support for other more active materials, in this case, fulfilling the role of a secondary electrocatalyst increasing selectivity toward desired products, while maintaining the catalytic properties of the primary catalyst.

The present work aims to study the role of Ti and Cu (primary components of electrodes) in NiRR toward  $\text{NH}_3$  and establish the optimal electrochemical conditions for maximizing its generation. Under those circumstances, electrochemical activity ( $\text{NO}_3^-$  reduction rate) and kinetic rate constants were evaluated in first place for the Ti electrode (Ti as the primary catalyst). In the second place, for  $\text{Cu}_2\text{O}$ –Cu titanium-modified electrode ( $\text{Cu}_2\text{O}$ –Cu/Ti), studying the synergistic effects on efficiency parameters of having Ti as active support for more active materials. In general, this work aims at demonstrating that the combination of materials with different intrinsic activities (i.e., Cu-based for higher activity for nitrate conversion; Ti for higher faradaic efficiency to ammonia) is a potential strategy to obtain synergistic effects in the direction of ammonia generation from nitrates. Therefore, productivity values of  $0.28 \text{ mmol}_{\text{NH}_3} \cdot \text{cm}^{-2} \cdot \text{h}^{-1}$  with  $\text{FE}_{\text{NH}_3} > 90\%$  at  $-0.5 \text{ V}$  vs RHE are demonstrated with the  $\text{Cu}_2\text{O}$ –Cu/Ti materials.

## EXPERIMENTAL SECTION

**Chemicals and Materials.** Titanium Foil (Ti), Copper Foil (Cu), Graphite Foil (Gr), and sodium carbonate ( $\text{NaCO}_3$ ) were supplied from Thermo Scientific Chemicals (Alfa-Aesar). Copper(II) chloride dihydrate ( $\text{CuCl}_2 \cdot 2\text{H}_2\text{O}$ ), potassium chloride, potassium hydroxide, ethanol, 2-propanol, and propanone were purchased from Sigma-Aldrich. Merck supplied potassium nitrate ( $\text{KNO}_3$ ), Nessler reagent, ammonium chloride ( $\text{NH}_4\text{Cl}$ ), and sodium hydrogen carbonate ( $\text{NaHCO}_3$ ).

**Electrode Preparation.** *Ti electrode.* Electrode preparation consisted of the chemical removal of impurities present on the Ti surface. First, the Ti foil was sonicated for 15 min in a solution of acetone, isopropyl alcohol, and ethanol in a proportion (1:1:1) for removal of organic and inorganic oils. Then, it was submerged in an acidic solution ( $\text{H}_2\text{SO}_4$  10% + citric acid  $36 \text{ g} \cdot \text{L}^{-1}$ ) under sonication for 5 min and finally rinsed in Milli-Q water for 10 min.

*Preparation of the  $\text{Cu}_2\text{O}$ –Cu/Ti Electrodes.*  $\text{Cu}_2\text{O}$ –Cu nanoparticles were plated by pulsed electrodeposition (PED) on a  $1 \times 1.5 \text{ cm}^2$  Ti Foil (99.5%, 0.25 mm thick) pretreated as previously described. This technique has been reported to allow for direct growth of shape-controlled  $\text{Cu}_2\text{O}$  nanocubes.<sup>30</sup> In principle, during the alternated potential conditions, Cu nuclei are formed with further material deposition, while noncubic particles are preferentially dissolved during the anodic cycles. A cyclic voltammetry measure-

ment (CV) was performed with the electrolyte  $5 \text{ mM CuCl}_2 + 5 \text{ mM KCl}$  (pH 6) for determining the optimal parameters of Cu electrodeposition and for its partial oxidation to  $\text{Cu}_2\text{O}$  onto Ti. Figure 1a shows the CV curve performed with a scan rate of  $10 \text{ mV} \cdot \text{s}^{-1}$ . The peaks situated at  $E_w -0.2$  and  $-0.8 \text{ V}$  vs  $\text{Ag}/\text{AgCl}_{3.5\text{M KCl}}$  are associated with reduction of  $\text{Cu}^{2+}$  to  $\text{Cu}^{1+}$  and reduction of  $\text{Cu}^{1+}$  to  $\text{Cu}^0$ , respectively.<sup>31</sup> As a result, the working potentials for PED were defined as  $-0.8 \text{ V}$  vs  $\text{Ag}/\text{AgCl}_{3.5\text{M KCl}}$  for depositing Cu nanoparticles and  $0.1 \text{ V}$  vs  $\text{Ag}/\text{AgCl}_{3.5\text{M KCl}}$  for the partial oxidation to  $\text{Cu}_2\text{O}$ .

The PED was performed using a BioLogic workstation with a three-electrode undivided cell equipped with a  $\text{Ag}/\text{AgCl}_{3.5\text{M KCl}}$  and Pt mesh as reference and counter electrode, respectively (Figure 1b). The applied potentials were  $E_{w,c} = -0.8 \text{ V}$ , during a duty time of 0.625 s, and  $E_{w,a} = 0.1 \text{ V}$ , during 7.5 s (Figure 1c) for a defined number of cycles ( $N = 30$ ). The optimum pH value for the PED and Cu nanoparticles stability was fixed in a range of 5.5–6 which is previous to the formation of copper hydroxide  $\text{Cu}(\text{OH})_2$  in the electrolyte.<sup>32</sup> Figure 1d shows the waveform of the chronoamperometry and the currents reached during the PED, with a cathodic current peak of  $-5.5 \text{ mA}$  where the Cu nanoparticles were expected to be deposited on the Ti support, and a later anodic peak current of  $0.1 \text{ mA}$  where the nanoparticles are expected to partially oxidize to  $\text{Cu}_2\text{O}$  onto the Cu surface. After PED, the  $\text{Cu}_2\text{O}$ –Cu/Ti electrodes were thoroughly rinsed with Milli-Q water ( $18.2 \text{ M}\Omega \cdot \text{cm}^{-1}$ ). Before all electrochemical experiments, the electrolyte was purged with  $\text{N}_2$  for 15 min. Fresh electrolyte was used for each PED in order to keep the initial concentration of the electroplating solution. All the depositions were made without stirring, and keeping a distance of 1 cm between counter and working electrodes.

$\text{Cu}_2\text{O}$ –Cu/Gr electrodes were prepared following the same procedure after an electrochemical evaluation of the required applied potentials.

**Electrodes Characterization.** The morphology of the copper nanoparticles and the Ti electrode surface were analyzed using FE-SEM (using a Field emission Zeiss Auriga series instrument) and energy-dispersive X-ray (EDX) analysis. X-ray diffraction patterns were also obtained by X-ray diffraction (XRD) in a D8 Advance Bruker equipment using  $\text{Cu K}\alpha$  radiation ( $\lambda = 1.5418 \text{ \AA}$ ). Raman spectroscopy was performed on an iHR320 spectrometer from HORIBA Scientific with a green laser ( $\lambda = 532 \text{ nm}$ ). In addition, other surface analysis techniques were performed on electrodes. The chemical and electronic states of the atoms in the electrode were analyzed by X-ray photoelectron spectroscopy (XPS) using a PHI instrument model 5773 Multitechnique with a  $\text{Al K}\alpha$  radiation ( $1486.6 \text{ eV}$ ).

**Electrochemical Measurements.** All electrochemical experiments were conducted at room temperature using a BioLogic electrochemical workstation. For the NiRR to ammonia tests, a three-electrode H-cell was used. A Nafion-117 cation exchange membrane divided the cathode and anode. A gas absorption liquid chamber was connected to the cathode compartment. A flow of  $\text{N}_2$  was passed through the cathode chamber (but not through the catholyte) dragging gaseous products, and a solution of  $1 \text{ mM H}_2\text{SO}_4$  was used to capture the ammonia in the headspace of the chamber. For the calculations, the total produced ammonia was the addition of the ammonia present in the electrolyte and that in the acidic trap. Figure S1 represents the electrochemical setup.

The prepared  $\text{Cu}_2\text{O}$ –Cu deposited on Ti and Gr Foils ( $1 \times 1 \text{ cm}^2 \times 2$  geometric areas in all cases) was used as working electrodes,  $\text{Ag}/\text{AgCl}_{3.5\text{M KCl}}$  as the reference electrode, and a Pt mesh served as the counter electrode. All potentials in chronoamperometry tests in this study are reported in V vs reversible hydrogen electrolyte (RHE), and the potential interconversion between electrodes is defined by  $E_{\text{RHE}} = E_{\text{Ag}/\text{AgCl}_{3.5\text{M KCl}}} + 0.205 \text{ V} + 0.059 \cdot \text{pH}$ . For NiRR studies, two electrolyte conditions were prepared with two extreme pH values. For acidic conditions, the electrolyte was  $0.3 \text{ M KNO}_3 + 0.1 \text{ M HNO}_3$  (final  $[\text{NO}_3^-]$  of  $0.4 \text{ M}$  and pH 1). While for the alkaline conditions, a solution consisting of  $0.1$ – $0.4 \text{ M KNO}_3$  and  $1 \text{ M KOH}$  was prepared, with a final pH of 14. The electrolyte for the electrochemical rate constant determination with the rotating disk electrode (RDE)

consisted of 0.01 M KNO<sub>3</sub> + 1 M KOH. The double layer capacitances were determined for Ti and Cu<sub>2</sub>O–Cu/Ti electrodes using a 0.1 M K<sub>2</sub>SO<sub>4</sub> electrolyte. Before the experiments, N<sub>2</sub> was bubbled through the electrolyte solution for 15 min to remove all the dissolved gases.

For the NiRR to NH<sub>3</sub> study, linear sweep voltammetry (LSV) was applied to all electrolyte conditions and all prepared electrodes in the potential window of 0 to –1 V vs RHE with a scan rate of 10 mV·s<sup>–1</sup>. Likewise, chronoamperometry tests were conducted with all prepared electrodes. The acidic electrolyte conditions were applied only for pure Ti electrodes due the low stability of Cu-based nanoparticles under those conditions. Faradaic efficiency (FE<sub>i</sub> toward NH<sub>3</sub>, NO<sub>2</sub><sup>–</sup>, and H<sub>2</sub>), selectivity (SE<sub>i</sub> toward NH<sub>3</sub>, and NO<sub>2</sub><sup>–</sup>), and productivity (NH<sub>3</sub> yield) were evaluated by chronoamperometries at –0.3, –0.4, –0.5, –0.6, –0.7, and –0.8 V vs RHE working potentials. These efficiency parameters were calculated as defined below:

$$FE_i(\%) = \frac{\alpha \cdot C_i \cdot F}{M \cdot Q} \cdot 100 \quad (1)$$

$$\text{NH}_3 \text{ yield (mmol cm}^{-2} \text{ h}^{-1}) = \frac{C_{\text{NH}_3} \cdot V \cdot M}{A \cdot t} \quad (2)$$

$$SE_i(\%) = \frac{C_i}{C_{\text{NO}_3^-} - C_{\text{NO}_3^0}} \cdot 100 \quad (3)$$

$C_i$  (M) is the obtained molar concentration of a target product;  $V$  (L) is the volume of electrolyte in the cathode chamber;  $M$  (g·mol<sup>–1</sup>) is the molar mass of the target product;  $A$  (cm<sup>2</sup>) is the geometric surface area of the electrode;  $\alpha$  is the number of transferred electrons for producing a target product;  $F$  is the Faraday constant,  $Q$  is the total charge transferred to the system;  $C_{\text{NH}_3}$  (M) is the measured NH<sub>3</sub> concentration for the reaction;  $t$  (h) represents the duration of chronoamperometry tests; and  $C_{\text{NO}_3^0}$  and  $C_{\text{NO}_3^-}$  (M) represent the initial and final concentration of nitrates in the electrolyte.

**Electrochemical Rate Constant  $k$ , Determination.** RDE LSV measures were performed at 0.5 V to –0.88 V vs RHE potential window for 0.01 M KNO<sub>3</sub> + 1 M KOH with a scan rate of 10 mV·s<sup>–1</sup> under the rotating rates 100, 300, 600, 1000, 1500, 2000 rpm. The kinetic currents of NiRR for the different electrode materials were determined by the Koutecky–Levich (K–L) analysis and the electrochemical rate constants by equations described in the SI.<sup>33</sup>

**Analytical Instrumentation and Measurements.** A gas chromatography equipment (GC, Agilent technologies 490 Micro GC) was used for quantification of H<sub>2</sub>, as a major gas product. The concentrations of NO<sub>3</sub><sup>–</sup> and NO<sub>2</sub><sup>–</sup> anions were measured by an Ion Chromatograph (Dionex 1100) equipped with a Dionex Ion Pac AS-22 anion exchange column and a chemical suppressor (ASR-ultra 4 mm), using 4.5 mM Na<sub>2</sub>CO<sub>3</sub> + 1.4 mM NaHCO<sub>3</sub> as eluent at 1.5 mL·min<sup>–1</sup>. The NH<sub>3</sub>/NH<sub>4</sub><sup>+</sup> concentration was determined by visible spectroscopy (after complexing NH<sub>4</sub><sup>+</sup> ions by Nessler reagent)<sup>35,36</sup> on a PerkinElmer Lambda-950 spectrometer. Hydrazine and hydroxylamine were not determined during electrochemical tests. The calibration curves and nitrate and nitrite ion peaks are shown in Figure S2.

## RESULTS AND DISCUSSION

**Characterization of Electrodes.** The phase composition of the Cu<sub>2</sub>O–Cu/Ti and Cu<sub>2</sub>O–Cu/Gr electrodes was studied by XRD, and the results are displayed in Figure 2. From Figure 2, a set of diffraction peaks at different positions can be seen. These peaks are indexed to the (1 0 0), (0 0 2), (1 0 1), (1 0 2), (1 1 0), (1 0 3), (2 0 0), (1 1 2), (2 0 1), (0 0 4), (2 0 2), and (1 0 4) lattice planes of Ti (JCPDS 00-044-1294). Additionally, a small diffraction peak corresponding to cuprite Cu<sub>2</sub>O (JCPDS 005-0667) can be also found. In Figure 2, the corresponding peaks of Cu<sup>0</sup> were imperceptible owing to the small amount of deposited Cu nanoparticles (charge equivalent

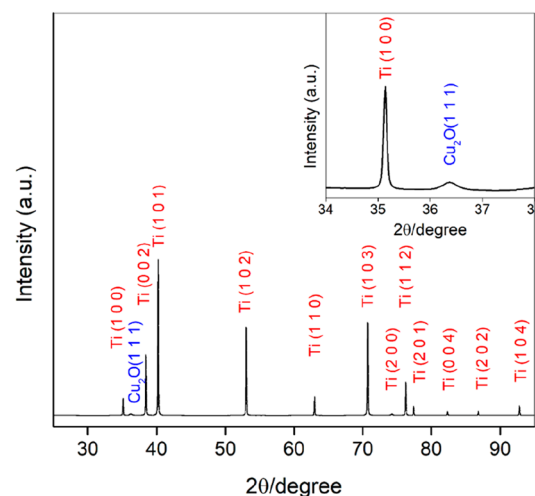


**Figure 2.** XRD results for the Cu<sub>2</sub>O–Cu/Ti electrode. In the inset graph, 2 $\theta$  range of 34° to 38°.

to 0.055 C) and the overlapping with high intensity peaks associated with Ti. However, an alternative route was employed for identifying the peaks of Cu<sub>2</sub>O–Cu nanoparticles depositing them onto a Gr foil support. Figure S3a shows the XRD diffraction patterns for the Cu<sub>2</sub>O–Cu/Gr electrode in which it was possible to identify two peaks at 36.7° and 43.298° associated with the lattice planes of Cu<sub>2</sub>O(111) and Cu(111) respectively (JCPDS 005-0667 and 004-0836). These results indicate the partial oxidation of the Cu nanoparticles during the PED, which was further confirmed by Raman and XPS analyses. Meanwhile, no other impurity peaks were observed on the XRD patterns of both electrodes. Raman spectroscopy measurements were also conducted on a Cu<sub>2</sub>O–Cu/Ti electrode, as shown in Figure S3b. As seen, peaks corresponding to several modes of Cu<sub>2</sub>O, CuO, and rutile TiO<sub>2</sub> can be found, in agreement with the results obtained by XRD.

Figure 3a,b shows the morphology of Cu<sub>2</sub>O–Cu/Ti electrodes observed by SEM before electrolysis. From the image, the irregular surface of Ti support can be seen homogeneously covered by Cu<sub>2</sub>O–Cu nanocrystals after PED. Under high magnification, it was observed a layer of cubic-like nanocrystals with sizes between of 40–80 nm (edge-to-edge). By recording an EDX spectrum (Figure S4a), the Cu<sub>2</sub>O–Cu/Ti electrode was estimated to have a qualitative atomic composition of 1.2% Cu, 86.5% Ti, and 12.2% C. Furthermore, XPS was used to identify the chemical species on the electrode surface. Figure 3c depicts the XPS spectrum in the Cu 2p region. The spectrum shows the two peaks corresponding to the 2p<sub>3/2</sub> and 2p<sub>1/2</sub> spin orbitals, along with the satellite peaks at 940–948 eV. The presence of these satellite peaks and their binding energies confirm the existence of oxidized Cu forms on the Cu<sub>2</sub>O–Cu/Ti electrode. The peak Cu 2p<sub>3/2</sub> was deconvoluted into two peaks, confirming the coexistence Cu<sup>+</sup> at 932.39 eV, Cu<sup>2+</sup> at 934.48 eV, and Cu<sup>0</sup> at 931.0 eV in the nanocubes. The ratios Cu<sup>+</sup>/total-Cu and Cu<sup>2+</sup>/total-Cu were determined to be 78% and 20%, respectively. The presence of Cu<sup>2+</sup> can be correlated with the oxidation process of the nanocubes by exposition to air prior to the XPS analysis. Figure 3d shows the Ti 2p spectrum. Two strong peaks appear at 458.4 and 464.1 eV that can be correlated with Ti<sup>4+</sup>, indicating the presence of superficial TiO<sub>2</sub> in the Cu<sub>2</sub>O–Cu/Ti electrode. A deconvolu-

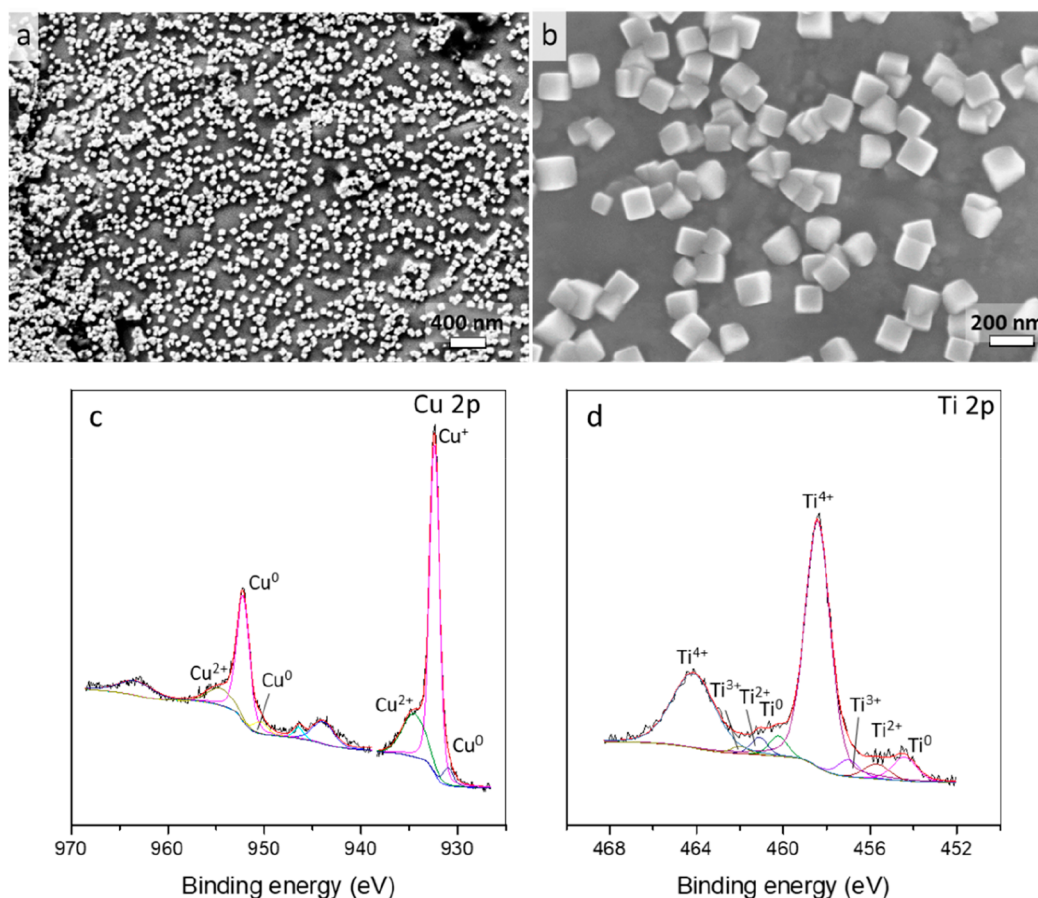


Figure 3.  $\text{Cu}_2\text{O-Cu/Ti}$  electrodes characterization: a, b) SEM images, c) Cu 2p, and d) Ti 2p XPS spectra.

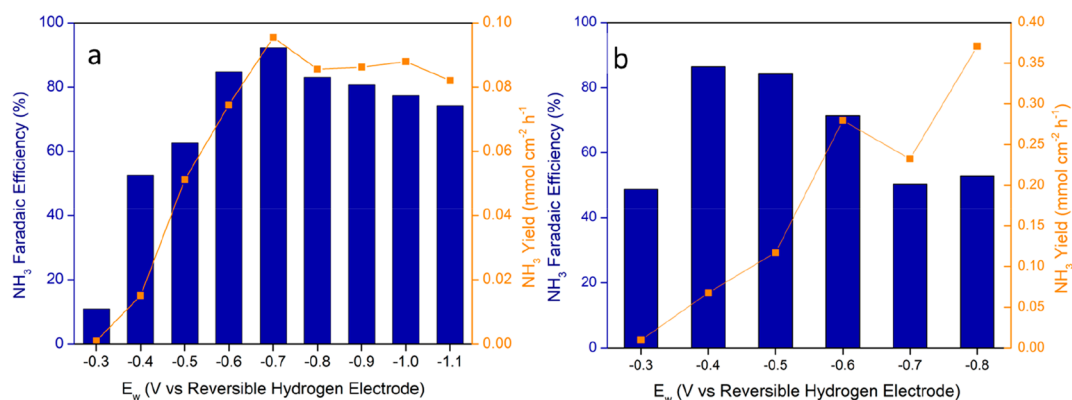
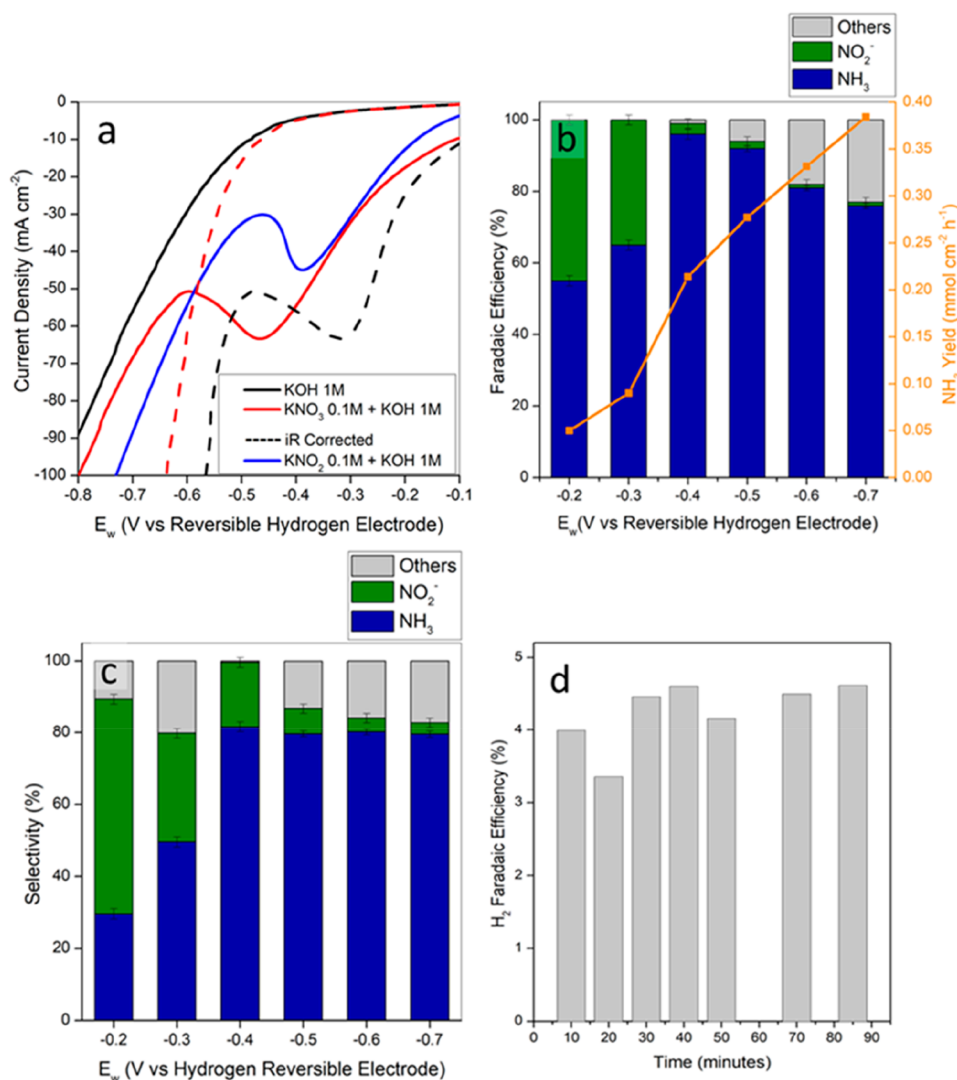


Figure 4.  $\text{FE}_{\text{NH}_3}$  and productivities for Ti electrode under a) acidic ( $0.3 \text{ M KNO}_3 + 0.1 \text{ M HNO}_3$ ) and b) alkaline conditions ( $0.1 \text{ M KNO}_3 + 1 \text{ M KOH}$ ).

tion of the peaks situated at 453–457 eV indicates as well the minor presence of other oxidized forms of Ti ( $\text{Ti}^{2+}$  and  $\text{Ti}^{3+}$  at 454.4 and 456.6 eV, respectively).<sup>37</sup> The Ti peak is situated at 453.71 eV. The Auger LMM spectrum for the  $\text{Cu}_2\text{O-Cu/Ti}$  electrode in Figure S3 also suggests the presence of copper in the form of  $\text{Cu}^+$  rather than as metallic  $\text{Cu}^0$ , as observed by the signal at 570 eV, associated with  $\text{Cu}^+$ .<sup>38</sup>

**Effects of pH and  $\text{NO}_3^-$  Concentration in NiRR Catalyzed by Ti Electrodes.** Several studies have correlated extreme pH conditions with higher nitrate conversion rates, FE or SE, or with higher  $\text{NH}_3$  productivities.<sup>28,31,34</sup> LSV curves

obtained with the Ti electrodes were recorded at pH 14 ( $0.4 \text{ M KNO}_3 + 1 \text{ M KOH}$ ) and pH 1 ( $0.3 \text{ M KNO}_3 + 0.1 \text{ M HNO}_3$ ) using a scan rate of  $10 \text{ mV}\cdot\text{s}^{-1}$  as illustrated in Figure S5. Polarization values between 0 V and  $-0.3 \text{ V}$  vs RHE showed low current densities for both electrolyte conditions. However, a sustained increment can be seen in the current density at alkaline conditions from  $-0.4 \text{ V}$  toward more negative potentials. A different behavior is observed under acidic conditions, where HER is highly suppressed by the high availability of  $\text{NO}_3^-$  ions that compete for the active sites with protons, conducting the reaction toward  $\text{NH}_3$ .<sup>39</sup> In the case of



**Figure 5.** Efficiency parameters for  $\text{Cu}_2\text{O-Cu@Ti}$  electrode: a) LSV and *iR* corrected LSV with different electrolyte compositions; b) FE,  $\text{yield}_{\text{NH}_3}$ ; c) SE at different operation voltages; d)  $\text{FE}_{\text{H}_2}$  vs time at  $E_w$   $-0.4$  V vs RHE, with  $0.1$  M  $\text{KNO}_3$  +  $1$  M KOH.

the alkaline electrolyte, HER seems to be limited by the low proton concentrations in the electrolyte along with the high concentration of  $\text{K}^+$  ions in solution. Monteiro et al. have observed a reduction in activity of HER at a high concentration of weakly hydrate ions such  $\text{K}^+$  in high alkaline solutions. This effect is mainly due to the blockage effect caused by the cation accumulation on the interface catalyst-solution.<sup>40,41</sup> Additionally, the high concentration of cations in solution can reduce the repulsive forces between cathode and  $\text{NO}_3^-$  enhancing NiRR to nitrogen-based products generation. The observed higher current densities at alkaline conditions can be correlated with a higher activity of pure Ti electrodes in NiRR in alkaline medium. This in turn can be associated with a higher  $\text{NO}_3^-$  reduction rate and/or higher product generation, something further observed during chronoamperometry tests. The effects on  $\text{NO}_3^-$  concentration were previously studied for pure Ti electrodes and other electrode materials.  $0.1$  M  $\text{NO}_3^-$  in the electrolyte was found as the concentration with the highest  $\text{FE}_{\text{NH}_3}$  and  $\text{SE}_{\text{NH}_3}$  at strong alkaline pH.<sup>28,42</sup> Further experiments with Ti and  $\text{Cu}_2\text{O-Cu/Ti}$  electrodes at alkaline conditions were carried out exclusively with  $0.1$  M  $\text{KNO}_3$  concentration.

The LSVs performed with Ti electrodes suggested a higher electrochemical activity in alkaline conditions, although the information about the efficiency of NiRR-to- $\text{NH}_3$  was provided by the chronoamperometry tests. Figure 4 displays the productivity ( $\text{NH}_3$  yield) and the faradaic efficiencies of NiRR to  $\text{NH}_3$  after 90 min. Figure 4a corresponds to a chronoamperometry carried out with  $0.3$   $\text{KNO}_3$  +  $0.1$  M  $\text{HNO}_3$  for the Ti electrode. The results agree with those already observed by McEnaney et al. under identical conditions where a maximum value of more than 90% of  $\text{FE}_{\text{NH}_3}$  was observed at  $-0.7$  V vs RHE, with 12% of  $\text{NO}_3^-$  conversion and  $\text{NH}_3$  yield of  $0.096$   $\text{mmol}\cdot\text{cm}^{-2}\cdot\text{h}^{-1}$ . Figure 4b, corresponds to the chronoamperometry performed with  $0.1$  M  $\text{KNO}_3$  +  $1$  M KOH and the Ti electrode, with the  $\text{FE}_{\text{NH}_3}$  also displaying a volcano shape with a maximum value at  $-0.4$  V vs RHE. In the case of alkaline conditions, the maximum observed at  $-0.4$  V vs RHE corresponds to a  $\text{FE}_{\text{NH}_3}$  of 86%. The productivity, however, continuously increases showing a  $\text{NH}_3$  yield  $0.37$   $\text{mmol}\cdot\text{cm}^{-2}\cdot\text{h}^{-1}$  at  $-0.8$  V vs RHE. The  $\text{NO}_3^-$  conversion rate was increased at more negative polarization voltages as shown in Figure S6. On one hand, the high  $\text{FE}_{\text{NH}_3}$  observed at acidic

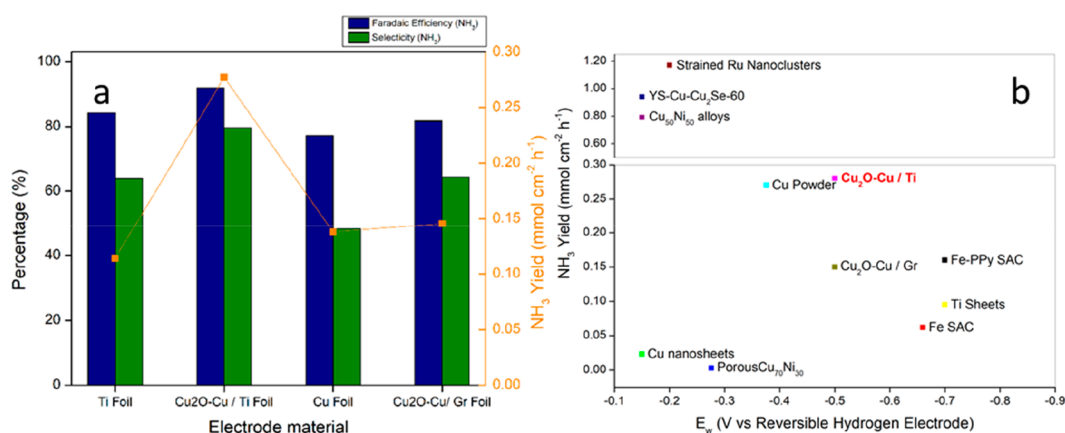


**Figure 6.** a) FE and productivity values for different cathode materials with 0.1 M KNO<sub>3</sub> + 1 M KOH at  $-0.5$  V vs RHE; b) NH<sub>3</sub> yield vs  $E_w$  comparison of different reported values and present work.<sup>21,28,42,48,51–53</sup>

conditions complements the information obtained in LSV curves. While the high KNO<sub>3</sub> concentration significantly suppresses the HER making possible to obtain a higher FE<sub>NH<sub>3</sub></sub>,<sup>43,44</sup> the low current densities reflected low productivities for all compared working potentials. Chen et al. have observed a lower interaction between NO<sub>3</sub><sup>−</sup> molecules and Ti active sites if compared with that observed for Cu active sites. This low interaction could be reflected in low current densities, compensated by the high concentration that limits parasite reactions such the HER. On the other hand, the low concentration of protons in solution at alkaline conditions limits the competition for the active sites with nitrate ions, increasing the FE<sub>NH<sub>3</sub></sub> at less negative potential values, while the higher currents observed by LSV were reflected in higher productivities.

**Performance of Cu<sub>2</sub>O–Cu on Different Supports.** Pure Ti electrodes have demonstrated catalytic properties to conduct efficiently the NiRR-to-NH<sub>3</sub> with limited productivity at low cathodic potentials. As mentioned previously, Cu<sub>2</sub>O-Cu nanocubes as part of a composite electrode, such as the synthesized Cu<sub>2</sub>O–Cu/Ti, can promote the RDS (NO<sub>3</sub><sup>−</sup> to NO<sub>2</sub><sup>−</sup>), while Ti might preserve its intrinsic NH<sub>3</sub> selectivity. Similar behavior has been observed by Cerrón-Calle et al. with a Cu–Pt bimetallic 3D-electrocatalyst where a synergistic effect between components of the electrocatalyst was reported.<sup>45</sup> As depicted in Figure 5a, in the presence of NO<sub>3</sub><sup>−</sup>, the voltammetric curves exhibit a broad peak between  $-0.3$  to  $-0.6$  V vs RHE, with a maximum at around  $-0.48$  V. An additional LSV with KNO<sub>2</sub> displays a narrower peak centered at around  $-0.39$  V. According to these results and to previous studies carried out with Cu-base electrodes, the former peak seems to encompass the initial conversion of NO<sub>3</sub><sup>−</sup> into NO<sub>2</sub><sup>−</sup> and the further reduction to NH<sub>3</sub>.<sup>21,34</sup> Figure 5b shows the FE values for the different products (in the liquid phase) for a series of chronoamperometries carried out at different working potentials:  $-0.2$ ,  $-0.3$ ,  $-0.4$ ,  $-0.5$ ,  $-0.6$ , and  $-0.7$  V vs RHE during a standard time of 90 min. The observed trend for FE<sub>NH<sub>3</sub></sub> followed a volcano shape with a maximum value of 96% at  $-0.4$  V vs RHE, after which decreased at more negative potentials. In general, the decline in FE<sub>NH<sub>3</sub></sub> is closely associated with the increased FE toward other reaction products (e.g., NO<sub>2</sub><sup>−</sup>, H<sub>2</sub>), as observed at low and higher polarization values. The evolution of H<sub>2</sub> was followed by gas chromatography, and the results are illustrated in Figure

5d for a 90 min chronoamperometry. At  $-0.4$  V vs RHE, the average FE<sub>H<sub>2</sub></sub> value remains relatively constant around 4% during the electrolysis time. These values are consistent with the measured FE for other products observed in the liquid phase. In the case of FE<sub>NO<sub>2</sub><sup>−</sup></sub>, the maximum values were reached at less negative potentials. As mentioned previously, several authors situate the first electron transfer of the NO<sub>3</sub><sup>−</sup>-to-NO<sub>2</sub><sup>−</sup> reaction as the RDS in the overall NiRR to any product, in which NO<sub>2</sub><sup>−</sup> is the first stable intermediate.<sup>46</sup> This implies that, at low polarization values, the lower kinetics of NiRR limits further NO<sub>2</sub><sup>−</sup> reduction allowing its desorption from the catalyst surface into the bulk electrolyte. The accumulation of NO<sub>2</sub><sup>−</sup> ions in the bulk continues as long as the concentration of NO<sub>3</sub><sup>−</sup> ions in the solution remains high. In line with this, as observed in Figure 5c, the SE<sub>NH<sub>3</sub></sub> shows a gradual increase with the cathodic potential. The peak value of 82% was observed at  $-0.4$  V vs RHE, similar to that achieved for the Ti electrode. However, a slight decline was observed at more negative potentials in the range of  $-0.5$  V to  $-0.7$  V vs RHE, achieving an average value of 80% in most cases. Less negative applied potentials ( $E_w = -0.2$  to  $-0.3$  V vs RHE) have shown higher NO<sub>2</sub><sup>−</sup> selectivity, with a maximum value of 60% obtained at  $-0.2$  V vs RHE. The accumulation of nitrite ions in the bulk electrolyte at these potentials is a consequence of the nature of the NiRR with the Cu-Cu<sub>2</sub>O/Ti electrode. This region presents the optimal electrochemical conditions for the conversion of NO<sub>3</sub><sup>−</sup> to NO<sub>2</sub><sup>−</sup>, in which the slow kinetics for the further reduction of NO<sub>2</sub><sup>−</sup> into NH<sub>3</sub> allows its accumulation.<sup>34,47</sup> In the case of productivity, expressed as yield (mmol<sub>NH<sub>3</sub></sub>·cm<sup>-2</sup>·h<sup>-1</sup>), the values were gradually increased as the cathodic potential became more negative as shown in Figure 5b, reaching up to 0.38 at  $-0.7$  V vs RHE. Despite the continuous increase of NH<sub>3</sub> productivity with the working voltage, there is an obvious detrimental effect on the FE at more negative potentials than  $-0.5$  V vs RHE. Therefore, considering the values of FE (92%), SE (80%), and yield (0.28 mmol·cm<sup>-2</sup>·h<sup>-1</sup>) to NH<sub>3</sub>, we consider an operation voltage around  $-0.4$  to  $-0.5$  V to be the optimum one to balance process efficiency and ammonia productivity.

NO<sub>3</sub><sup>−</sup> conversion and specific conversion rates are presented in Figure S6. The percentage of removed nitrate was increased at more negative potentials up to 75% ( $-0.8$  V vs RHE) for both Ti and Cu<sub>2</sub>O-Cu/Ti electrodes. However, the specific rate is expressed in mg<sub>NO<sub>3</sub><sup>−</sup></sub>·C<sup>-1</sup>, which indicates the amount of

nitrate removed by unit of charge decreased progressively at more negative potentials due the contribution of HER. A value of  $0.093 \text{ mg}_{\text{NO}_3^-} \cdot \text{C}^{-1}$  was observed at  $-0.5 \text{ V}$  vs RHE for the  $\text{Cu}_2\text{O}-\text{Cu}/\text{Ti}$  electrode. The specific  $\text{NO}_3^-$  degradation can give information regarding which type of material can offer better properties for denitrification of waters. While Ti electrodes showed slightly better nitrate specific degradation (another way to measure its efficiency), the composite electrodes showed remarkably higher activity in terms of absolute  $\text{NO}_3^-$  degradation at less negative potentials. Thus,  $\text{Cu}_2\text{O}-\text{Cu}$  nanoparticles seem to increase the activity of the Ti electrode with a slight sacrifice of the efficiency in terms of specific degradation and selectivity to ammonia at lower polarization values.

In order to determine the effect of the substrate,  $\text{Cu}_2\text{O}-\text{Cu}/\text{Gr}$  electrodes were evaluated under similar conditions, and the FE and productivity values are presented in Figure S7. The  $\text{FE}_{\text{NH}_3}$  peak of 82% is situated at  $-0.5 \text{ V}$  vs RHE, and the  $\text{NH}_3$  yield increased at higher negative potentials up to  $0.36 \text{ mmol}$  within the studied working potentials. The peak of  $\text{FE}_{\text{NO}_2^-}$  16% was observed at  $-0.4 \text{ V}$ , and FE to other products such  $\text{H}_2$  was higher at more cathodic potentials. At the same applied potential ( $-0.5 \text{ V}$  vs RHE), the  $\text{Cu}_2\text{O}-\text{Cu}/\text{Gr}$  electrode showed similar  $\text{FE}_{\text{NH}_3}$  and higher productivity (expected for Cu-based electrodes) values than the pure Ti electrode. However, these values were notoriously lower than the ones obtained with  $\text{Cu}_2\text{O}-\text{Cu}/\text{Ti}$ , confirming the synergistic effects between components Ti and Cu in the composite electrode.

Figure 6a shows a comparison of different cathode materials at  $-0.5 \text{ V}$  vs RHE for NiRR to  $\text{NH}_3$  with  $0.1 \text{ M KNO}_3 + 1 \text{ M KOH}$  electrolyte. Pure Cu, Ti, and composite  $\text{Cu}_2\text{O}-\text{Cu}/\text{Ti}$  and  $\text{Cu}_2\text{O}-\text{Cu}/\text{Gr}$  electrodes were compared in terms of  $\text{FE}_{\text{NH}_3}$ ,  $\text{SE}_{\text{NH}_3}$ , and productivity. As previously studied, the high selectivity of pure Ti electrode for reducing  $\text{NO}_3^-$  to  $\text{NH}_3$  (contrary to their low catalytic activity) makes it an excellent active support for NiRR catalysts such Cu-based materials. FE and/or SE decrease in electrodes without Ti in the structure. As shown in Figure S8, this effect is more obvious at a less negative potential of  $-0.4 \text{ V}$ , where the selectivity and productivity to  $\text{NH}_3$  diminish with the  $\text{Cu}_2\text{O}-\text{Cu}/\text{Gr}$  electrode, thus suggesting a role of Ti support. Additionally, the partially oxidized nature of Cu-based nanoparticles in the  $\text{Cu}_2\text{O}-\text{Cu}/\text{Gr}$  electrode leads to a slightly increased selectivity toward  $\text{NH}_3$  if compared with a pure Cu electrode at  $-0.5 \text{ V}$ . The  $\text{Cu}_2\text{O}-\text{Cu}/\text{Ti}$  electrode takes advantage of the intrinsic properties of the components, causing a synergistic effect that promotes ammonia generation, as demonstrated by the  $\text{NH}_3$  yield values.

Figure 6b displays  $\text{NH}_3$  productivities reported in the literature for different cathode materials. According to our best knowledge, Li et al. have reported the highest  $\text{NH}_3$  productivity for NiRR ( $1.17 \text{ mmol} \cdot \text{cm}^{-2} \cdot \text{h}^{-1}$ ) using a strained Ru nanocluster electrode and high alkaline conditions ( $1 \text{ M NaNO}_3 + 1 \text{ M NaOH}$ ).<sup>48</sup> This is followed by the productivity value reported by Wang et al. ( $0.79 \text{ mmol} \cdot \text{cm}^{-2} \cdot \text{h}^{-1}$ ) with a  $\text{Cu}_{50}\text{Ni}_{50}$  alloy catalyst under alkaline conditions ( $0.1 \text{ M KNO}_3 + 1 \text{ M KOH}$ ) performed with a flow cell.<sup>42</sup> The productivity reached in this work has surpassed other reported for pure Cu-based or more complex-structure composite electrodes by adjusting electrochemical conditions and with a less-complex synthesis method.

Additionally, stability tests were performed with the  $\text{Cu}_2\text{O}-\text{Cu}/\text{Ti}$  electrode under alkaline conditions by applying several cycles on the same sample. Every cycle consisted of a 90 min chronoamperometry at  $-0.4 \text{ V}$  vs RHE with fresh electrolyte. As observed in Figure S9, the  $\text{FE}_{\text{NH}_3}$  remains higher than 90% for three different cycles. On the contrary, productivity values resulted slightly affected after the first cycle, decreasing in around 20% with respect to the initial  $\text{NH}_3$  yield, although it was practically retained for the third one. This decrease in productivity can be a consequence of changes in morphology of  $\text{Cu}_2\text{O}-\text{Cu}$  nanocubes as observed in Figure S4b after the chronoamperometry test.

**Rotating Disk Electrode Study.** In order to evaluate the kinetic performance of the materials involved in this work for NiRR, estimation of the electrochemical rate constants ( $k_i$ ) was carried out with rotating disk electrode (RDE) measurements, complemented with calculation of double layer capacitances ( $C_{\text{DL}}$ ). A detailed description on the conditions, setup, and calculations is included in the SI. From the LSV and K-L plots in Figure S10, electrochemical rate constant values are estimated from the extracted kinetic current, leading to a value of  $3.91 \times 10^{-4} \text{ cm} \cdot \text{s}^{-1}$  for the  $\text{Cu}_2\text{O}-\text{Cu}/\text{Ti}$  disk electrode. This value is the same order of magnitude as a reported  $k_i^0$  for NiRR of  $2.48 \times 10^{-4} \text{ cm} \cdot \text{s}^{-1}$  of an electrodeposited Cu-Pt electrode under neutral pH.<sup>49</sup> The  $k_i$  of Cu and Ti disk electrodes were estimated by the same procedure, leading to values of  $3.88 \times 10^{-4}$  and  $3.02 \times 10^{-6} \text{ cm} \cdot \text{s}^{-1}$ , respectively. The performance of the  $\text{Cu}_2\text{O}-\text{Cu}/\text{Ti}$  electrode at low potential values (between  $-0.4$  to  $-0.6 \text{ V}$  vs RHE) seems to maintain the characteristics of the pure Ti electrode, such as the high FE and SE to  $\text{NH}_3$ . However, a high activity in NiRR related to Cu-based electrodes stands out. The similar  $k_i$  measured for the  $\text{Cu}_2\text{O}-\text{Cu}/\text{Ti}$  and Cu disk electrodes can serve as a reference for understanding the higher activity of the Cu-modified Ti electrodes with respect to pristine Ti under the specified conditions.

Estimation of  $C_{\text{DL}}$  values for the  $\text{Cu}_2\text{O}-\text{Cu}/\text{Ti}$  and Ti electrodes has been carried out, in order to study the influence of surface area on the efficiency parameters. For this purpose, cyclic voltammograms were recorded at different scan rates in neutral electrolyte, as described and represented in Figure S11.  $C_{\text{DL}}$  values of 120 and  $150 \mu\text{F}$  for  $\text{Cu}_2\text{O}-\text{Cu}/\text{Ti}$  and Ti electrodes were obtained, respectively, for  $1 \text{ cm}^2$  geometric area. This similarity of  $C_{\text{DL}}$  values can be correlated to similar electrochemical surface areas between the two electrodes, which suggests that no significant surface variation occurs on the Ti surface in terms of active area. Moreover, with further attempts to determine a  $k_i$  value by considering an additional parameter to reduce the error caused by the use of a geometric flat area (see SI), a slightly higher electrochemical rate constant of  $4.77 \times 10^{-4} \text{ cm} \cdot \text{s}^{-1}$  is obtained for the  $\text{Cu}_2\text{O}-\text{Cu}/\text{Ti}$  disk electrode.

Previous studies have found synergistic effects when Cu surfaces/particles were partially oxidized to  $\text{Cu}^+$ , in which the presence of metallic copper can accelerate the reaction rate of the RDS, while the  $\text{Cu}^+$  particles can conduct further reductions selectively to  $\text{NH}_3$ .<sup>22,50</sup> In fact, the increased  $k_i$  demonstrates that combining  $\text{Cu}_2\text{O}-\text{Cu}$  nanoparticles with Ti surfaces could offer a better kinetic behavior for NiRR-to- $\text{NH}_3$  than the pure elements. While the combination of metallic and partial oxidized Cu ( $\text{Cu}_2\text{O}$ ) enhances the catalytic activity and reduces the required potential of pristine Cu for NiRR-to- $\text{NH}_3$ ,

Ti confers stability, limits HER, and efficiently conducts NiRR to NH<sub>3</sub> as the final product.

## CONCLUSION

Electrochemical reduction of nitrate toward ammonia using Ti, electrodeposited Cu<sub>2</sub>O-Cu/Ti, and Cu<sub>2</sub>O-Cu/Gr cathodes have been investigated in an H-type divided and with rotating disk electrodes in a series of electrolyte conditions. In general, pristine Ti electrodes showed excellent properties as supporting active material for NiRR, being highly sensitive to the NO<sub>3</sub><sup>-</sup> concentration and pH of the electrolyte. Higher current densities were obtained under alkaline conditions, which is translated into higher catalytic activity for NiRR. Acidic conditions showed higher FE toward NH<sub>3</sub> (90%) than alkaline conditions (82%) at their respective optimal working potential, with lower productivities.

Cu<sub>2</sub>O-Cu/Ti electrodes efficiently conduct the NiRR-to-NH<sub>3</sub> process allowing working at an optimum potential of -0.5 V vs RHE, attaining FE<sub>NH<sub>3</sub></sub> and SE<sub>NH<sub>3</sub></sub> values of 92 and 80%, respectively. The composite electrode showed synergistic properties with respect to individual components (high faradaic efficiency toward NH<sub>3</sub> of pristine Ti and high NiRR activity of copper and copper oxide nanoparticles).

The estimated electrochemical rate constants ( $k_i$ ) resulted in similar values for pure Cu and Cu<sub>2</sub>O-Cu/Ti disk electrodes ( $3.88 \times 10^{-4}$  and  $3.91 \times 10^{-4}$  cm·s<sup>-1</sup> respectively). However, the correction of the disk geometric areas with the  $\psi$  factor increased the  $k_i$  of the composite electrode up to  $4.77 \times 10^{-4}$  cm·s<sup>-1</sup> pointing to an improved kinetic performance of combined Cu<sub>2</sub>O and Ti. In this sense, the present work shows that combining materials with different intrinsic activities is a good strategy to boost productivity, while preserving the efficiency toward the desired product.

## ASSOCIATED CONTENT

### Supporting Information

The Supporting Information is available free of charge at <https://pubs.acs.org/doi/10.1021/acssuschemeng.2c05885>.

NO<sub>3</sub><sup>-</sup>, NO<sub>2</sub><sup>-</sup>, and NH<sub>3</sub>/NH<sub>4</sub><sup>+</sup> calibration curves; setup schematic; additional XRD results, Raman and XPS spectra; SEM and EDX spectra; LSV curves at different conditions; overall and specific nitrate conversions at varied working potentials; additional performance and stability tests for different electrodes; RDE study; double layer capacitance determination (PDF)

## AUTHOR INFORMATION

### Corresponding Author

Sebastián Murcia-López – Catalonia Institute for Energy Research (IREC), Sant Adrià de Besòs 08930, Spain;  
✉ [orcid.org/0000-0002-3703-041X](mailto:smurcia@irec.cat); Email: [smurcia@irec.cat](mailto:smurcia@irec.cat)

### Authors

Marcelo Eduardo Chavez – Catalonia Institute for Energy Research (IREC), Sant Adrià de Besòs 08930, Spain  
Martí Biset-Peiró – Catalonia Institute for Energy Research (IREC), Sant Adrià de Besòs 08930, Spain  
Joan Ramon Morante – Catalonia Institute for Energy Research (IREC), Sant Adrià de Besòs 08930, Spain;  
Facultat de Física, Universitat de Barcelona, Barcelona 08028, Spain

Complete contact information is available at:  
<https://pubs.acs.org/10.1021/acssuschemeng.2c05885>

## Notes

The authors declare no competing financial interest.

## ACKNOWLEDGMENTS

The authors thank Generalitat de Catalunya for financial support through the CERCA Program, M2E (2017SGR1246). IREC also acknowledges support from the European Regional Development Funds (ERDF, FEDER) and by MCIN/AEI/10.13039/501100011033 CERES project (PID2020-116093RB-C42). M.E.C. acknowledges the Formacion Profesional de Investigadores Program (PRE2018-083575) and the Becas Carlos Antonio Lopez (BECAL) Program (82/2019).

## REFERENCES

- (1) Brandon, N. P.; Kurban, Z. Clean energy and the hydrogen economy., *Philos. Trans. R. Soc. A Math. Phys. Eng. Sci.* **2017**, *375* (2098), 20160400.
- (2) Brightling, J. Ammonia and the fertiliser industry: The development of ammonia at Billingham., *Johnson Matthey Technol. Rev.* **2018**, *62* (1), 32–47.
- (3) Valera-Medina, A.; Xiao, H.; Owen-Jones, M.; David, W. I. F.; Bowen, P. J. Ammonia for power., *Prog. Energy Combust. Sci.* **2018**, *69*, 63–102.
- (4) Ayvali, T.; Edman Tsang, S. C.; Van Vrijaldenhoven, T. The position of ammonia in decarbonising maritime industry: An overview and perspectives: Part I: Technological. *Johnson Matthey Technol. Rev.* **2021**, *65* (2), 275–290.
- (5) Makepeace, J.; He, T.; Weidenthaler, C.; Jensen, T. R.; Chang, F.; Vegge, T.; Ngene, P.; Kojima, Y.; de Jongh, P. E.; Chen, P.; David, W. Reversible ammonia-based and liquid organic hydrogen carriers for high-density hydrogen storage: Recent progress., *Int. J. Hydrogen Energy* **2019**, *44* (15), 7746–7767.
- (6) Lasocki, J.; Bednarski, M.; Sikora, M. Simulation of ammonia combustion in dual-fuel compression-ignition engine., *IOP Conf. Ser. Earth Environ. Sci.* **2019**, *214* (1), 012081.
- (7) Smith, C.; Hill, A. K.; Torrente-Murciano, L. Current and future role of Haber-Bosch ammonia in a carbon-free energy landscape., *Energy Environ. Sci.* **2020**, *13* (2), 331–344.
- (8) Rouwenhorst, K. H. R.; Engelmann, Y.; Van 'T Veer, K.; Postma, R. S.; Bogaerts, A.; Lefferts, L. Plasma-driven catalysis: Green ammonia synthesis with intermittent electricity., *Green Chem.* **2020**, *22* (19), 6258–6287.
- (9) Kim, H. H.; Teramoto, Y.; Ogata, A.; Takagi, H.; Nanba, T. Plasma Catalysis for Environmental Treatment and Energy Applications., *Plasma Chem. Plasma Process.* **2016**, *36* (1), 45–72.
- (10) Zhao, R.; Xie, H.; Chang, L.; Zhang, X.; Zhu, X.; Tong, X.; Wang, T.; Luo, Y.; Wei, P.; Wang, Z.; Sun, X. Recent progress in the electrochemical ammonia synthesis under ambient conditions., *EnergyChem.* **2019**, *1* (2), 100011.
- (11) Cao, Y.; Li, P.; Wu, T.; Liu, M.; Zhang, Y. Electrocatalysis of N<sub>2</sub> to NH<sub>3</sub> by HKUST-1 with High NH<sub>3</sub> Yield., *Chem.- An Asian J.* **2020**, *15* (8), 1272–1276.
- (12) Shalev, N.; Burg, A.; Gavrieli, I.; Lazar, B. Nitrate contamination sources in aquifers underlying cultivated fields in an arid region - The Arava Valley, Israel., *Appl. Geochem.* **2015**, *63*, 322–332.
- (13) Paredes, I.; Otero, N.; Soler, A.; Green, A. J.; Soto, D. X. Agricultural and urban delivered nitrate pollution input to Mediterranean temporary freshwaters., *Agric. Ecosyst. Environ.* **2020**, *294* (February), 106859.
- (14) Calle-Vallejo, F.; Huang, M.; Henry, J. B.; Koper, M. T. M.; Bandarenka, A. S. Theoretical design and experimental implementation of Ag/Au electrodes for the electrochemical reduction of nitrate., *Phys. Chem. Chem. Phys.* **2013**, *15* (9), 3196–3202.

- (15) Marchesini, F. A.; Aghemo, V.; Moreno, I.; Navascués, N.; Irusta, S.; Gutierrez, L. Pd and Pd<sub>2</sub>In nanoparticles supported on polymer fibres as catalysts for the nitrate and nitrite reduction in aqueous media., *J. Environ. Chem. Eng.* **2020**, *8* (2), 103651.
- (16) Fajardo, A. S.; Westerhoff, P.; Sanchez-Sanchez, C. M.; Garcia-Segura, S. Earth-abundant elements a sustainable solution for electrocatalytic reduction of nitrate., *Appl. Catal. B Environ.* **2021**, *281* (June 2020), 119465.
- (17) Wang, J.; Ling, L.; Deng, Z.; Zhang, W. Nitrogen-doped iron for selective catalytic reduction of nitrate to dinitrogen., *Sci. Bull.* **2020**, *65* (11), 926–933.
- (18) Jonoush, Z. A.; Rezaee, A.; Ghaffarinejad, A. Electrocatalytic nitrate reduction using FeO/Fe<sub>3</sub>O<sub>4</sub> nanoparticles immobilized on nickel foam: Selectivity and energy consumption studies., *J. Clean. Prod.* **2020**, *242*, 118569.
- (19) Lan, Y.; Chen, J.; Zhang, H.; Zhang, W.-x.; Yang, J. Fe/Fe<sub>3</sub>C nanoparticle-decorated N-doped carbon nano fibers for improving the nitrogen selectivity of electrocatalytic nitrate reduction †., *J. Mater. Chem. A Mater. energy Sustain.* **2020**, *8*, 15853.
- (20) Marcos-Hernandez, M.; Antonio Cerron-Calle, G.; Ge, Y.; Garcia-Segura, S.; Sanchez-Sanchez, C. M.; Fajardo, A. S.; Villagran, D. Effect of surface functionalization of Fe<sub>3</sub>O<sub>4</sub> nano-enabled electrodes on the electrochemical reduction of nitrate., *Sep. Purif. Technol.* **2022**, *282* (July 2021), 119771.
- (21) Fu, X.; Zhao, X.; Hu, X.; He, K.; Yu, Y.; Li, T.; Tu, Q.; Qian, X.; Yue, Q.; Wasielewski, M.; Kang, Y. Alternative route for electrochemical ammonia synthesis by reduction of nitrate on copper nanosheets., *Appl. Mater. Today* **2020**, *19*, 100620.
- (22) Fu, W.; Hu, Z.; Zheng, Y.; Su, P.; Zhang, Q.; Jiao, Y.; Zhou, M. Tuning mobility of intermediate and electron transfer to enhance electrochemical reduction of nitrate to ammonia on Cu<sub>2</sub>O/Cu interface., *Chem. Eng. J.* **2022**, *433* (October), 133680.
- (23) Chen, G.; Yuan, Y.; Jiang, H.; Ren, S.; Ding, L.; Ma, L.; Wu, T.; Lu, J.; Wang, H. Electrochemical reduction of nitrate to ammonia via direct eight-electron transfer using a copper-molecular solid catalyst., *Nat. Energy* **2020**, *5*, 605.
- (24) Shih, Y. J.; Wu, Z. L.; Lin, C. Y.; Huang, Y. H.; Huang, C. P. Manipulating the crystalline morphology and facet orientation of copper and copper-palladium nanocatalysts supported on stainless steel mesh with the aid of cationic surfactant to improve the electrochemical reduction of nitrate and N<sub>2</sub> selectivity., *Appl. Catal. B Environ.* **2020**, *273* (May), 119053.
- (25) Gao, W.; Gao, L.; Li, D.; Huang, K.; Cui, L.; Meng, J.; Liang, J. Removal of nitrate from water by the electrocatalytic denitrification on the Cu-Bi electrode., *J. Electroanal. Chem.* **2018**, *817* (April), 202–209.
- (26) Zhang, Y.; Zhao, Y.; Chen, Z.; Wang, L.; Wu, P.; Wang, F. Electrochemical reduction of nitrate via Cu/Ni composite cathode paired with Ir-Ru/Ti anode: High efficiency and N<sub>2</sub> selectivity., *Electrochim. Acta* **2018**, *291*, 151–160.
- (27) Feng, T.; Wang, J.; Wang, Y.; Yu, C.; Zhou, X.; Xu, B.; László, K.; Li, F.; Zhang, W. Selective electrocatalytic reduction of nitrate to dinitrogen by Cu<sub>2</sub>O nanowires with mixed oxidation-state., *Chem. Eng. J.* **2022**, *433*, 133495.
- (28) McEnaney, J.; Blair, S.; Niender, A.; Schwalbe, J.; Koshy, D.; Cargnello, M.; Jaramillo, T. F. Electrolyte engineering for efficient electrochemical nitrate reduction to ammonia on a titanium electrode., *ACS Sustain. Chem. Eng.* **2020**, *8* (7), 2672–2681.
- (29) Jia, R.; Wang, Y.; Wang, C.; Ling, Y.; Yu, Y.; Zhang, B. Boosting Selective Nitrate Electroreduction to Ammonium by Constructing Oxygen Vacancies in TiO<sub>2</sub>., *ACS Catal.* **2020**, *10* (6), 3533–3540.
- (30) Grosse, P.; Yoon, A.; Rettenmaier, C.; Chee, S. W.; Roldan Cuenya, B. Growth Dynamics and Processes Governing the Stability of Electrodeposited Size-Controlled Cubic Cu Catalysts., *J. Phys. Chem. C* **2020**, *124* (49), 26908–26915.
- (31) Reyter, D.; Bélanger, D.; Roué, L. Elaboration of Cu-Pd films by coelectrodeposition: Application to nitrate electroreduction., *J. Phys. Chem. C* **2009**, *113* (1), 290–297.
- (32) Hidmi, L.; Edwards, M. Role of temperature and pH in Cu(OH)<sub>2</sub> solubility., *Environ. Sci. Technol.* **1999**, *33* (15), 2607–2610.
- (33) Sun, Y.; Li, S.; Jovanov, Z. P.; Bernsmeier, D.; Wang, H.; Paul, B.; Wang, X.; Kühl, S.; Strasser, P. Structure, “Structure, Activity, and Faradaic Efficiency of Nitrogen-Doped Porous Carbon Catalysts for Direct Electrochemical Hydrogen Peroxide Production., *ChemSusChem* **2018**, *11* (19), 3388–3395.
- (34) Reyter, D.; Bélanger, D.; Roué, L. Study of the electroreduction of nitrate on copper in alkaline solution., *Electrochim. Acta* **2008**, *53* (20), 5977–5984.
- (35) Zhao, Y.; Shi, R.; Bian, X.; Zhou, C.; Zhao, Y.; Zhang, S.; Wu, F.; Waterhouse, G.; Wu, L.; Tung, C.; Zhang, T. Ammonia Detection Methods in Photocatalytic and Electrocatalytic Experiments: How to Improve the Reliability of NH<sub>3</sub> Production Rates?., *Adv. Sci.* **2019**, *6* (8), 1802109.
- (36) Jeong, H.; Park, J.; Kim, H. Determination of NH<sub>4</sub><sup>+</sup> in environmental water with interfering substances using the modified nessler method., *J. Chem.* **2013**, *2013*, 1.
- (37) Biesinger, M. C.; Lau, L. W. M.; Gerson, A. R.; Smart, R. S. C. Resolving surface chemical states in XPS analysis of first row transition metals, oxides and hydroxides: Sc, Ti, V, Cu and Zn., *Appl. Surf. Sci.* **2010**, *257* (3), 887–898.
- (38) Zhu, C.; Osherov, A.; Panzer, M. J. Surface chemistry of electrodeposited Cu<sub>2</sub>O films studied by XPS., *Electrochim. Acta* **2013**, *111*, 771–778.
- (39) Krzywda, P. M.; Paradelo Rodríguez, A.; Cino, L.; Benes, N. E.; Mei, B. T.; Mul, G. Electroreduction of NO<sub>3</sub><sup>-</sup> on tubular porous Ti electrodes., *Catal. Sci. Technol.* **2022**, *12*, 3281–3288.
- (40) Monteiro, M. C. O.; Goyal, A.; Moerland, P.; Koper, M. T. M. Understanding Cation Trends for Hydrogen Evolution on Platinum and Gold Electrodes in Alkaline Media., *ACS Catal.* **2021**, *11* (23), 14328–14335.
- (41) Goyal, A.; Koper, M. T. M. Understanding the role of mass transport in tuning the hydrogen evolution kinetics on gold in alkaline media., *J. Chem. Phys.* **2021**, *155* (13), 134705.
- (42) Wang, Y.; Xu, A.; Wang, Z.; Huang, L.; Li, J.; Li, F.; Wicks, J.; Luo, M.; Nam, D.; Tan, C.; Ding, Y.; Wu, J.; Lum, Y.; Dinh, C.; Sinton, D.; Zheng, G.; Sargent, Edward H. Enhanced Nitrate-to-Ammonia Activity on Copper-Nickel Alloys via Tuning of Intermediate Adsorption., *J. Am. Chem. Soc.* **2020**, *142* (12), 5702–5708.
- (43) Cui, Z.; Ge, F.; Lin, Y.; Wang, L.; Lei, L.; Tian, H.; Yu, M.; Wang, X. Corrosion behavior of AZ31 magnesium alloy in the chloride solution containing ammonium nitrate., *Electrochim. Acta* **2018**, *278* (3), 421–437.
- (44) De Groot, M. T.; Koper, M. T. M. The influence of nitrate concentration and acidity on the electrocatalytic reduction of nitrate on platinum., *J. Electroanal. Chem.* **2004**, *562* (1), 81–94.
- (45) Cerrón-Calle, G. A.; Fajardo, A. S.; Sánchez-Sánchez, C. M.; Garcia-Segura, S. Highly reactive Cu-Pt bimetallic 3D-electrocatalyst for selective nitrate reduction to ammonia., *Appl. Catal. B Environ.* **2022**, *302*, 120844.
- (46) Duca, M.; Koper, M. T. M. Powering denitrification: The perspectives of electrocatalytic nitrate reduction., *Energy Environ. Sci.* **2012**, *5* (12), 9726–9742.
- (47) Wang, Y.; Wang, C.; Li, M.; Yu, Y.; Zhang, B. Nitrate electroreduction: Mechanism insight: In situ characterization, performance evaluation, and challenges., *Chem. Soc. Rev.* **2021**, *50* (12), 6720–6733.
- (48) Li, J.; Zhan, G.; Yang, J.; Quan, F.; Mao, C.; Liu, Y.; Wang, B.; Lei, F.; Li, L.; Chan, A.; Xu, L.; Shi, Y.; Du, Y.; Hao, W.; Wong, P.; Wang, J.; Dou, S.; Zhang, L.; Yu, J. Efficient Ammonia Electrosynthesis from Nitrate on Strained Ruthenium Nanoclusters., *J. Am. Chem. Soc.* **2020**, *142* (15), 7036–7046.
- (49) Mumtaz, Z.; Rahman, M. M.; Marwani, H. M.; Hasnat, M. A. Electro-kinetics of conversion of NO<sub>3</sub><sup>-</sup> into NO<sub>2</sub><sup>-</sup> and sensing of nitrate ions via reduction reactions at copper immobilized platinum surface in the neutral medium., *Electrochim. Acta* **2020**, *346*, 135994.

(50) Ren, T.; Ren, K.; Wang, M.; Liu, M.; Wang, Z.; Wang, H.; Li, X.; Wang, L.; Xu, Y. Concave-convex surface oxide layers over copper nanowires boost electrochemical nitrate-to-ammonia conversion. *Chem. Eng. J.* **2021**, *426* (June), 130759.

(51) Wu, Z.; Karamad, M.; Yong, X.; Huang, Q.; Cullen, D.; Zhu, P.; Xia, C.; Xiao, Q.; Shakouri, M.; Chen, F.; Kim, J.; Xia, Y.; Heck, K.; Hu, Y.; Wong, M.; Li, Q.; Gates, L.; Siahrostami, S.; Wang, H. Electrochemical ammonia synthesis via nitrate reduction on Fe single atom catalyst. *Nat. Commun.* **2021**, *12* (1), 1–10.

(52) Comisso, N.; Cattarin, S.; Guerriero, P.; Mattarozzi, L.; Musiani, M.; Vazquez-Gomez, L.; Verlato, E. Study of Cu, Cu-Ni and Rh-modified Cu porous layers as electrode materials for the electroanalysis of nitrate and nitrite ions. *J. Solid State Electrochem.* **2016**, *20* (4), 1139–1148.

(53) Li, P.; Jin, Z.; Fang, Z.; Yu, G. A single-site iron catalyst with preoccupied active centers that achieves selective ammonia electro-synthesis from nitrate. *Energy Environ. Sci.* **2021**, *14* (6), 3522–3531.